Formation, characterization and magnetic properties of maghemite γ-Fe₂O₃ nanoparticles in borate glasses

I.S. Edelman [a,*], O.S. Ivanova [a], E.A. Petrakovskaja [a], D.A. Velikanov [a,b], I.A. Tarasov [a], Y.V. Zubavichus [c], N.N. Trofimova [c], V.I. Zaikovskii [d,e]

[a] L.V. Kirensky Institute of Physics, Siberian Branch of the RAS, 660036 Krasnoyarsk, Russia
[b] Siberian Federal University, 660036 Krasnoyarsk, Russia
[c] NRC "Kurchatov Institute", 123182 Moscow, Russia
[d] Boreskov Institute of Catalysis, Siberian Branch of RAS, 630090 Novosibirsk, Russia
[e] Novosibirsk State University, 630090 Novosibirsk, Russia

ABSTRACT

A new type of nanocomposite materials based on maghemite, γ-Fe₂O₃, nanoparticles dispersed in borate glasses co-doped with low contents of iron together with the larger radius element combinations: Y and Bi, or Sm and Pb, or Y and Pb is studied. Nanoparticles arise as a result of heat treatment of the glasses which gives them properties characteristic of magnetically ordered substances. Transmission electron microscopy and XRD show that only one magnetic phase, namely γ-Fe₂O₃ nanoparticles, occurs in glasses subjected to the thermal treatment at 540 °C during 24 h independently on the doping element nature. At the same time doping element and their concentrations ratio in every combination affect the particles average size and glass magnetic properties, such as magnetization temperature dependences, Faraday rotation value and electron magnetic resonance spectrum characteristics.

© 2014 Elsevier B.V. All rights reserved.

1. Introduction

Physical and chemical properties stability is one of the important requirements to ensembles of magnetic nanoparticles for the production of functional materials [1]. A diamagnetic glassy matrix is quite appropriate host to protect the nanoparticles' surface and thus conserve their unique physical characteristics. Glasses doped with paramagnetic ions were the subjects of numerous studies over a few last decades. At sufficiently high concentration of doping elements, magnetic nanoparticles arise in glasses, typically upon a deliberate thermal treatment [2,3]. At that, glasses lose their transparency in the visible range. However, some glass systems admit magnetic nanoparticles precipitation even at low doping levels and thus preserve transparency in a red part of the visible and near infrared spectral ranges. In particular, borate glasses comply with that requirement. For example, nanoparticles of lithium ferrite LiFe₅O₈ in lithium borate glass containing less than one wt. percentage Fe₂O₃ [4,5] or maghemite γ-Fe₂O₃ nanoparticles in silica-gel glasses [6] were identified by electron magnetic resonance (EMR). In potassium–alumina–borate glasses co-doped with iron and manganese or with iron and cobalt, nanoparticles of manganese or cobalt ferrite, correspondingly, were detected with different

techniques [7,8] starting from 1.5 wt. percentage of Fe₂O₃ and 1.0 wt. percentage of MnO or CoO in the glass synthesis load. As it was shown in series of works (i.e., [9]), interesting results can be obtained when doping oxides glasses with Fe and rare earth (RE) simultaneously. That is why we used RE and some other large-ion-radius elements as co-dopants in order to maximize the magneto-optical activity of potassium–alumina–germanium–borate glasses. Nanoparticles arising in these glasses co-doped with iron and Dy, Tb, Gd, Ho, Er, Y, and Bi were shown to have the γ-Fe₂O₃ structure independently on co-dopant nature [10]. At the same time, nanoparticle morphology and dimensions, as well as the magnetic and magneto-optical characteristics of these particles containing samples differ strongly for different co-dopants and heat treatment regimes. The present paper is aimed to elucidate the role of the large-radius-ions elements in determining of the γ-Fe₂O₃ nanoparticles characteristics and on the glass magnetic properties for a series of glasses co-doped with Fe and large-ion-radius elements Y, Bi, Pb, Sm in different combinations subjected to the specific thermal treatment.

2. Experimental

Glasses of the basic composition K₂O–Al₂O₃–GeO₂–B₂O₃ were synthesized using a technique described in Ref. [7]. Prior to the synthesis, Fe₂O₃ and co-doping element oxides, i.e., Y₂O₃, Bi₂O₃, PbO, Sm₂O₃ in different combinations were loaded

---

in the charge in respective concentrations of ca. 3.0 and 0.0–4.0 wt.% with respect to basic glass composition. The mixtures were molten at 1100–1300 °C under oxidizing conditions. The melts were poured onto steel sheets, cooled down naturally to 380 °C in air and then kept at this temperature for several hours. Glass plates obtained in such a way were cut into several pieces which were subjected to additional thermal treatment at the same conditions at 540 °C during 24 h. The concentrations of the co-doping element oxides in the glass samples studied are listed in Table 1.

The visualization of particles formed in the glasses was carried out using electron microscope JEM-2200FS (JEOL Ltd.) operating in high resolution (HRTEM) and high-angle annular dark-field scanning (STEM-HAADF) transmission modes. Energy dispersive X-ray analysis (EDX) was used for identification of chemical compositions of glasses. Lattice spacing of crystalline impurities were measured by Fast Fourier transform (FFT) with the help of Digital Micrograph 3.3.1 (Gatan Ltd.). For the electron microscopic studies, the samples were finely ground, dispersed in ethanol, and deposited onto perforated carbon substrates attached to a standard copper grid and placed into the microscope UHV chamber.

The XRD analysis was done at the "Structural Materials Science" beamline [11] in the Kurchatov Synchrotron Radiation Centre (Moscow, Russia). The X-ray diffraction data were acquired in the transmission (Debye–Scherer) mode at a wavelength $\lambda = 0.696585$ Å using a 2D Fuji Film Imaging Plate detector; the sample-to-detector distance was 150 mm and the exposure time was about 20 min per sample.
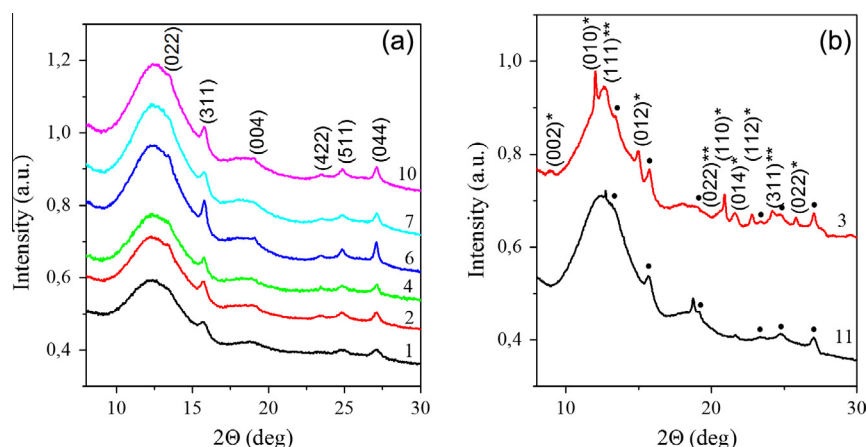
The magneto-optical measurements were made with 0.05 mm thick glass plates mechanically polished to optical roughness. The Faraday rotation (FR) was measured using zero method with an accuracy of ±0.1 min. The FR sign was determined with respect to the FR signal of a high-purity quartz sample taken as positive, as usually accepted. The magnetic circular dichroism (MCD) was measured by modulating the light polarization with an elastic-optical modulator as a difference (Δk) between the absorption values for the light waves clockwise (k_+) and counter-clockwise (k_-) polarized with respect to the direction of an external magnetic field normal to the sample plane. The FR and MCD spectra were measured in the energy range of 10000–22000 cm^{-1} in the magnetic field of 0.25 T. The accuracy of MCD measurements was ca. 10^{-4} cm^{-1}, and the spectral resolution was ca. 50 cm^{-1}.

The magnetization (M) was measured with a Quantum Design PPMS_9 instrument in the temperature range from 5 to 320 K, in magnetic field up to 12 T. The EMR spectra were recorded in the X band (9.46 GHz) with a Bruker EMX spectrometer equipped with an ER4112HV variable-temperature unit.

3. Results and discussion

3.1. Structural characterization

The XRD patterns for all glass samples show broad halos arising from the vitreous matrix and series of relatively narrow peaks. According to the peak positions, the XRD patterns can be formally classified into two groups. First group (A): patterns containing only peaks of maghemite γ-Fe_2O_3 (space group $P4_13_2$, $a = 8.351$ Å, PDF #39-1346), several examples are shown in Fig. 1a. The second group (B) samples are characterized by patterns containing other crystalline phases in addition to maghemite: precipitates consist of base matrix components $K_2Al_2B_2O_7$ and glasses with precipitates of Bi_2O_3, YBO_3 and unidentified phase, probably one of lead oxides PbO_x. XRD pattern for the representative examples of the B group is shown in Fig. 1b. Phase compositions for all samples are given in Table 1.

The positions of the maghemite peaks remain nearly the same for all samples whereas their relative intensities and widths depend on the co-dopant element concentrations. As shown in Table 1, these peaks can be indexed on a cubic lattice with parameter a in the range of 8.263–8.312 Å. The average nanoparticles

Table 1
Characteristics of glasses containing Bi, Y, Pb, Sm oxides in wt.% according to X-ray fluorescence analysis; crystal phases detected in the samples; γ-Fe_2O_3 cubic lattice parameter (a, Å); average crystallite size (d, nm); maghemite nanoparticles mass concentration (C, wt.%); relative FR value at $\lambda = 700$ nm (~ 14290 cm^{-1}) in $B = 0.25$ T. The FR value for sample 10 equal 6.5 deg/cm was taken as a unity.

Sample number	Large-ion-radius additives				Precipitates	a	d	C	The FR values
	Bi_2O_3	Y_2O_3	PbO	Sm_2O_3					
1	3.0	1.6	–	–	γ-Fe_2O_3	8.263	7.6	1.7	0.84
2	2.8	1.5	–	0.39	γ-Fe_2O_3	8.270	9.6	1.9	0.80
3	2.6	1.4	–	–	γ-Fe_2O_3 + Bi_2O_3 + YBO_3	8.309	11.6	1.8	0.82
4	2.2	1.1	–	–	γ-Fe_2O_3	8.294	11.3	1.4	0.97
5	–	–	0.7	0.3	γ-Fe_2O_3 + x + xx[*]	8.306	9.1	1.7	0.63
6	–	–	1.3	0.3	γ-Fe_2O_3	8.312	12.6	1.7	0.83
7	–	–	2.6	0.3	γ-Fe_2O_3	8.296	9.2	1.6	0.55
8	–	–	3.5	0.3	γ-Fe_2O_3 + PbO + x[*]	8.299	8.0	1.9	0.58
9	–	1.5	0.7	0.3	γ-Fe_2O_3	8.284	7.8	1.6	0.70
10	–	1.5	1.3	0.4	γ-Fe_2O_3	8.303	10.4	1.6	1
11	–	1.5	2.6	–	γ-Fe_2O_3 + PbO + x[*]	8.311	7.7	1.9	0.67
12	–	1.5	4.0	–	γ-Fe_2O_3 + $K_2Al_2B_2O_7$	8.296	8.7	1.8	0.61

[*] x and xx are unidentified Fe-free nonmagnetic phases.

Fig. 1. (a) X-ray diffraction patterns for the samples containing only maghemite crystal phase Nos. 1, 2, 4, 6, 7, and 10; (b) for the samples of the group B containing other crystalline phases besides maghemite (●): No. 11 probably containing PbO_x and No. 3 containing YBO_3 (peaks marked as $(hkl)^*$) and Bi_2O_3 peaks marked as $(hkl)^{**}$).

size, the lattice parameter and weight concentration for the γ-Fe_2O_3 phase were determined with the Rietveld refinement of XRD patterns (Fig. 2). The amorphous halos were described by split Pseudo-Voight peaks, crystalline phases were simulated based on available crystallographic data. Lattice parameters, size of crystallites and scale factors were fitted in the refinement procedure.
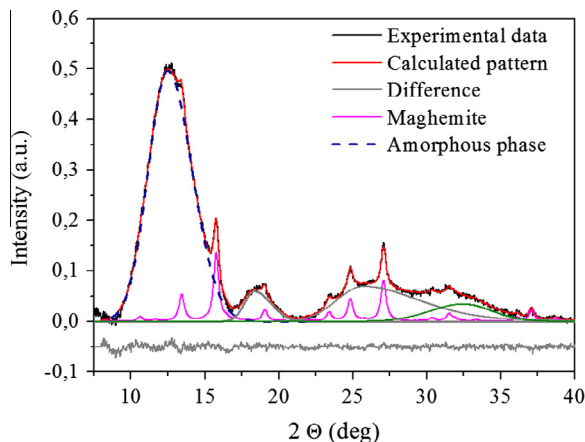

Fig. 2. Example of Rietveld refinement results for sample No. 6. (For interpretation of the color lines in this figure, the reader is referred to the web version of this article.)

The weight concentration of maghemite nanoparticles was estimated as a ratio of integral intensities of peaks belonging to maghemite and glass halos similar to the definition of crystallinity degree used for semi-crystalline polymers. Background was fitted by a fourth-order polynom. Results of five independent calculations were averaged.

Typical STEM-HAADF images of nanoparticles in a glass matrix are shown in Fig. 3a and b. For the majority of samples, aggregates composed of several particles up to 5–20 nm in size are observed. Sometimes, particles are aggregated and aligned into chains. Nanoparticles demonstrate crystalline structure; according to the HRTEM data (Fig. 3c) the lattice spacing of crystallites can be identified with FFT as maghemite, γ-Fe_2O_3, in compliance with the XRD data. STEM-EDX analysis was used to estimate the doping elements presence in different parts of a sample. Two examples are shown in Fig. 4a and b. Areas around particles and areas containing no particles are singled out by squares and designated by numbers. The EDX spectrum is shown in Fig. 5 for the 009 square. The elemental composition for all squares shown in Fig. 4-a and b for sample No. 2 is presented in Table 2.

EDX technique cannot detect the presence of boron, so the sum of all signals in the EDX spectrum was taken as 100%, and the separate signal of each element was considered in relation to it. As the particles were capsulated in the glass matrix, elements composing the matrix were detected in the EDX spectrum in each case. Therefore in the area of the particles they also defined, but in much smaller quantities. It is seen that all Fe is gathered in the particles,
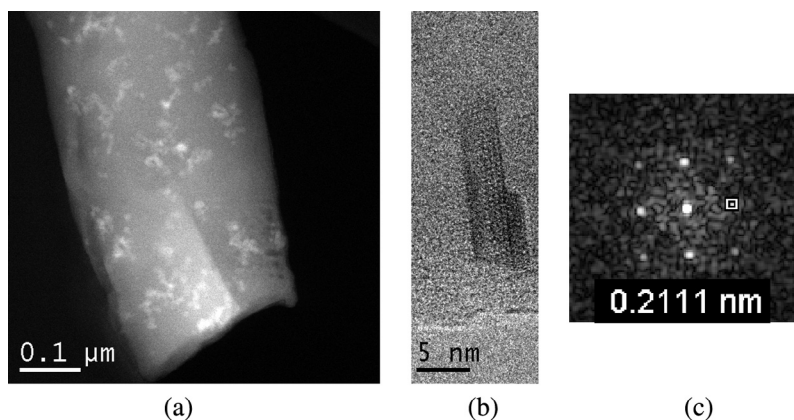

Fig. 3. (a) STEM-HAADF image of glass No. 1 fragment. (b) [0 0 1] projection of a single particle of maghemite, γ-Fe_2O_3. (c) FFT pattern of the single particle, reflections are closed to spacing d_{400}.
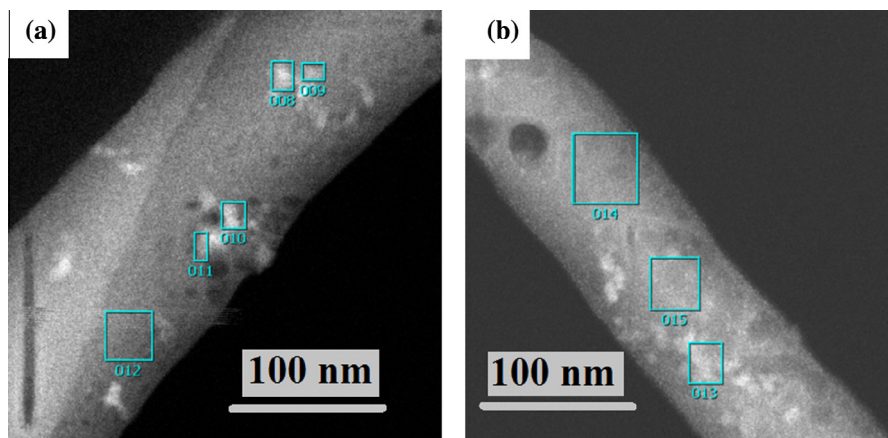

Fig. 4. STEM-HAADF images of different areas of the sample No. 2(a) and (b).
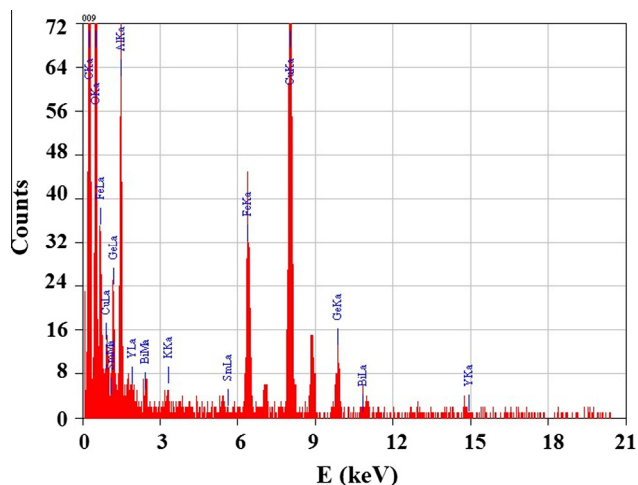
Fig. 5. EDX spectrum of the area marked by 009 in Fig. 4-a.

in areas containing no particles (012, 014) Fe absents. Interesting situation turns out with the spatial distribution of large radius ions. The Y, and Sm are clearly seen to be located in the nanoparticle areas. Bismuth, on the contrary, is observed in the areas free of particles and in the particles area it presents in the vanishingly small amount.

The data presented allow making a statement that Fe ions enter inside the particles, the Y and Sm ions are situated either inside the particles or form something like particle shell. The core–shell particles morphology was considered by several authors, in particular, Lembke et al. [12] inferred the existence of a nonmagnetic surface layer surrounding a magnetically ordered magnetite core basing on the small X-ray and neutron scattering results. Note, that RE ions prefer to form their own phases. A series of samples of the system $NiGd_xFe_{2-x}O_4$ ($x = 0, 0.1, 0.3, 0.5$ and 0.7) were investigated in Ref. [13]. The X-ray analysis showed that the samples with $x = 0$ and 0.1 were of spinel phase, but in samples with $x = 0.3$ and 0.5 the second inter-granular phase (orthorhombic, containing Gd) arises along with the spinel one. In Ref. [14] it was shown that the substitution of iron in the nickel zinc ferrites by rare-earth cations resulted in the formation of various rare-earth iron oxides. The rare-earth additions form various secondary phases, preferentially, rare-earth iron oxides. In Ref. [15], the $CoLn_{0.12}Fe_{1.88}O_4$ nanoparticles structure and magnetic properties were investigated in dependence on the RE nature (Ce, Sm, Eu, Gd, Dy, or Er). X-ray diffraction studies indicated all the Ln^{3+} ions to replace the octahedral Fe^{3+} ions only and the introduction of the small amount of lanthanide ions did not give a detectable change in the lattice constant and patterns were virtually identical to the pattern of ferrite nanoparticles. In our case only one magnetic phase has been detected, γ-Fe_2O_3, independently of the large radius ions nature. Bi and Pb are situated in regions free of particles and consequently can affect

in the process of the particles formation but not in their magnetic and magneto-optical properties. The mechanism of such an influence is not yet clear; this result seems to be quite consistent with results of Ref. [16] where the introduction of ErF_3 or SmF_3 into Na_2O–K_2O–BaF_2–BaO–Al_2O_3–SiO_2 glasses gave rise to a droplet phase separation upon heat treatment whereas no phase segregation occurred in undoped glasses. As for Y and Sm, the data obtained are not enough to determine unambiguously their exact location in the particle region.
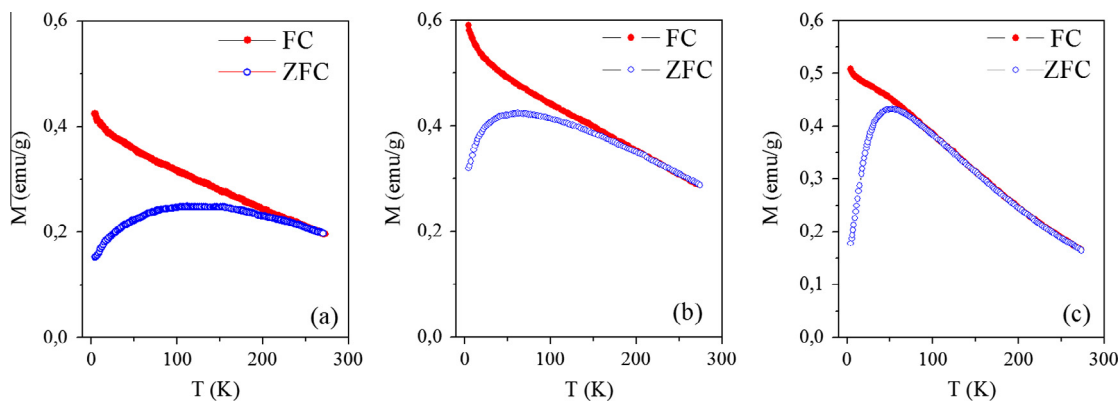
3.2. Magnetization

The magnetization temperature dependences were obtained in the course of samples heating after cooling in two different regimes: at presence of an external magnetic field (FC) and without magnetic field (ZFC). Several representative examples are shown in Fig. 6 for the FC and ZFC modes. For all samples, FC and ZFC curves are significantly different which is typical of superparamagnetic nanoparticles with blocking temperatures (T_b) over a wide range from ∼20 to 150 K depending on the nanoparticle size: the larger particles are blocked at higher temperatures up to the room temperature. Besides, the ZFC curves are characterized with the different maximum width for different samples. Broad maxima in ZFC curves can be explained by the dispersion of particles size.

Room temperature magnetization field dependence is shown in Fig. 7a for sample No. 2 together with the curve calculated according to the Langevin law taking into account the mean particle size from XRD. Though there is no hysteresis in the experimental curve, the discrepancy between the measured and calculated curves is observed that can be due to a wide distribution of particles size. At low temperatures, hysteresis loops occur, coercive field does not exceed 0.02 T at 4.2 K (Fig. 7b). Noteworthy, there is a difference between low temperature hysteresis loops measured for samples cooled in two regimes, viz., FC and ZFC. The FC loop demonstrates a vertical shift similar to that observed in nanostructured Fe/MnO_2 [17], Fe/CoO [18] nanocomposites. Authors of the cited references considered this shift to be due to spins pinned at the interface between ferromagnetic and antiferromagnetic components. Authors of Ref. [19] observed analogous vertical shifts of the FC loops at low temperatures for core–shell Fe/γ-Fe_2O_3 nanoparticles and ascribed it to the spin-glass-like phase of an oxide shell at low temperatures. In Ref. [20] vertical hysteresis loop shift was observed in the ensemble of NiO nanoparticle, and the shift value depended on the nanoparticles dimension. To explain our results, the approach developed in Ref. [18] seems to be most appropriate. Spin configuration can be different in the core and in the surface area of homogeneous ferrite particles because of different surroundings of magnetic atoms. Under ZFC conditions, the surface spins are orientated randomly in the whole temperature interval and, therefore, do not contribute to the core magnetization behavior. Under FC conditions the surface spins are frozen along the applied magnetic field and give the constant contribution to the sample magnetization independent on the switching field

Table 2
The elemental composition (in atom%) in different areas of sample No. 2, obtained from EDX spectra. The sum of all signals intensity in the EDXA spectrum was taken as 100%.

The square's number	Al	K	Ge	Fe	Bi	Y	Sm	Total (Atom%)
008	34.41	4.21	16.67	40.63	0.10	2.71	1.27	100.00
009	46.17	1.18	18.37	30.79	0.67	2.28	0.54	100.00
010	23.04	0.00	3.91	62.31	0.00	5.90	4.84	100.00
011	63.45	0.00	30.04	5.55	0.43	0.25	0.28	100.00
012	74.92	1.62	22.15	0.54	0.77	0.00	0.00	100.00
013	46.80	6.80	14.65	29.75	0.22	0.00	1.78	100.00
014	66.68	12.34	20.16	0.00	0.82	0.00	0.00	100.00
015	61.95	9.07	21.04	3.54	0.66	3.74	0.00	100.00

Fig. 6. Magnetization *vs.* temperature curves for FC and ZFC modes of several samples: No. 6 with the average particles size 12.6 nm (a), No. 4 with the average particles size 11.3 nm (b), No. 2 with the average particles size 9.6 nm (c).
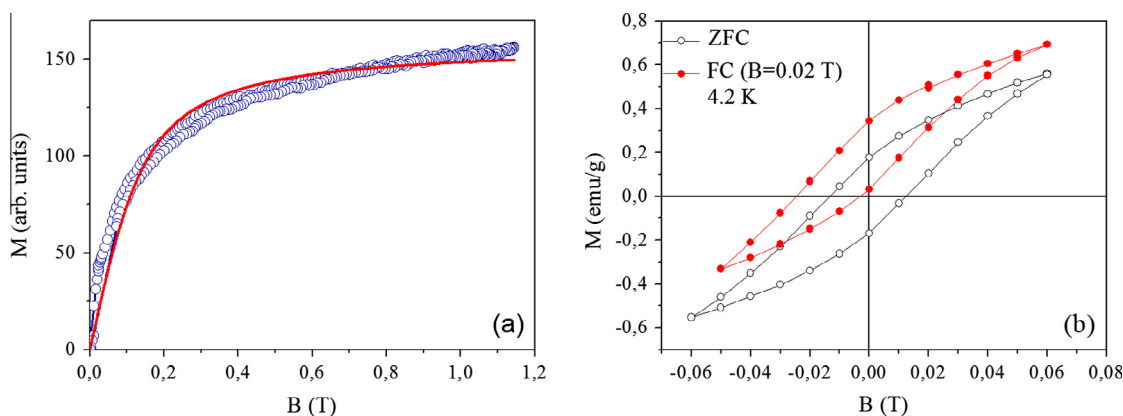
Fig. 7. (a) Room-temperature magnetization curve for sample No. 2 (circles) and Langevin fitted curve (solid line). (b) Hysteresis loops for sample No. 10 measured at *T* = 4.2 K under FC and ZFC cooling.

direction. At the opposite magnetic field direction during the FC process, the hysteresis loop shifts to opposite direction.

### 3.3. Magnetic circular dichroism

A typical MCD spectrum is shown in Fig. 8a for sample No. 12. Two overlapping peaks in the visible region and a broad weak peak of the opposite sign in the infrared (IR) region are the main features of the spectrum. For all other samples, spectra have virtually the same shape, but the peak intensities vary slightly from sample to sample. Peculiarities are observed also in absorption spectra (Fig. 8b) in the region of two first MCD peaks. Positions of peaks in the MCD spectrum correspond to energies of electron transitions between the ground and excited states of Fe^{3+} ion belonging to the $3d^5$ electron configuration. Since the energy of such transitions is determined by the crystal field (CF) value produced by atomic surrounding of the magnetic ion, the MCD spectrum is a powerful tool for identifying the crystal structure. That is why the MCD spectra can be considered as additional confirmation of the attributing of nanoparticle structure to γ-Fe_2O_3 structure suggested from SAED and XRD. So, the nature of magnetic nanoprecipitates in all glass samples investigated is independent on the co-dopant.

3.4. Faraday rotation

Similarly to MCD, shape of the FR spectra is nearly identical for all samples; observed differences in the effect value of different samples relates to the size and morphology of nanoparticles. Typical FR spectrum is shown in Fig. 9. A strong increase in FR signal

occurs at the wave length above 18000 cm^{-1}. Two kinks are seen in the FR curve at wavelength corresponding to energies of the MCD peaks (compare Figs. 8a and 9a). A wide weak maximum with a fine structure is observed in the IR region centered at $\sim$14290 cm^{-1} ($\sim$700 nm). This peak also corresponds to the IR MCD feature. A similar IR maximum of FR signal was observed in Ref. [21] for γ-Fe_2O_3 nanoparticles of 20 nm average size dispersed in silica matrix (the particles concentration was 18 wt.%). The authors [21] paid special attention to narrow peaks centered at 13070, 13620, 12670, and 12120 cm^{-1} superimposed on the wide maximum. Our spectrum also reveals some fine structure but not as distinct, possibly, because of a wider distribution of particle sizes and shapes. The sufficiently high FR signal in a combination with the low optical absorption in the vicinity of $\lambda \approx$ 700 nm (14290 cm^{-1}) make the glasses investigated highly promising for magneto-optical applications in the near IR spectral range.
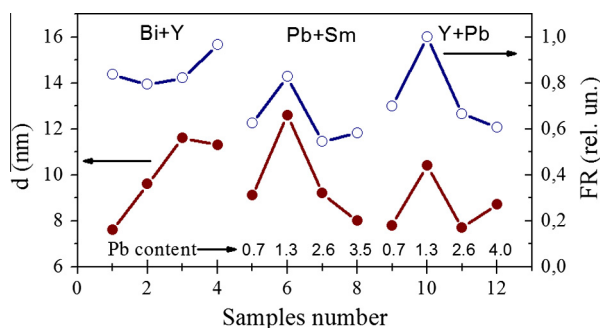
The FR values at 700 nm (14290 cm^{-1}) for all samples are collected in Table 1 in relative units. The peculiar correlation can be noted between FR value and nanoparticles size that depends, in turn, on the large radius ion additions combination. As it is seen in Fig. 10, for each set of the large radius ions (Bi and Y, Pb and Sm, Y and Pb) there is the ratio of components providing the largest particles size. The same behavior is observed for the FR value, the maximal value corresponds to the maximal particles size in each composition. Thus, there is a tendency in the magneto-optic parameters to be dependent on the particles dimension within the same composition. But there is some discrepancy between FR and particles size: among three compositions the highest FR maximum value is observed in sample No. 10 containing nanoparticles
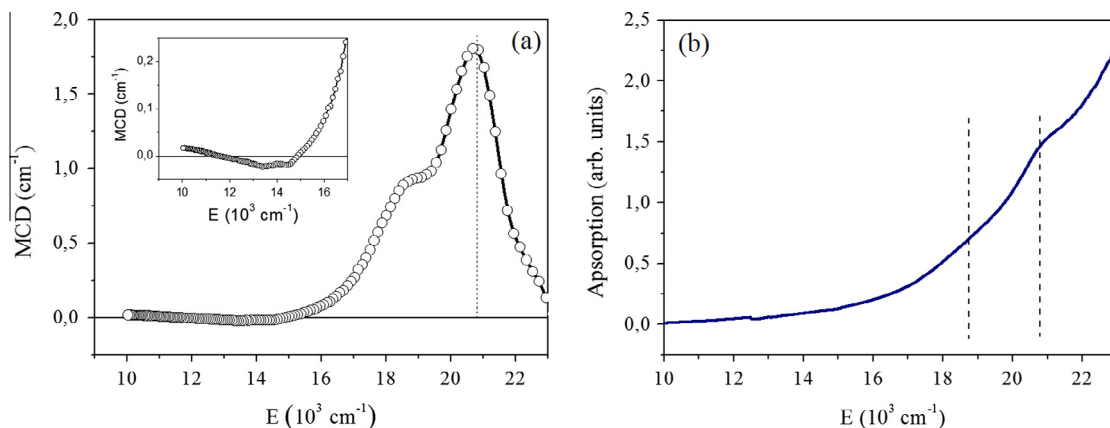
Fig. 8. (a) Room-temperature MCD spectrum of sample No. 12. Inset: IR spectral range. (b) Absorption spectrum of sample No. 4. Dashed vertical lines mark positions of peaks observed in the MCD spectrum.
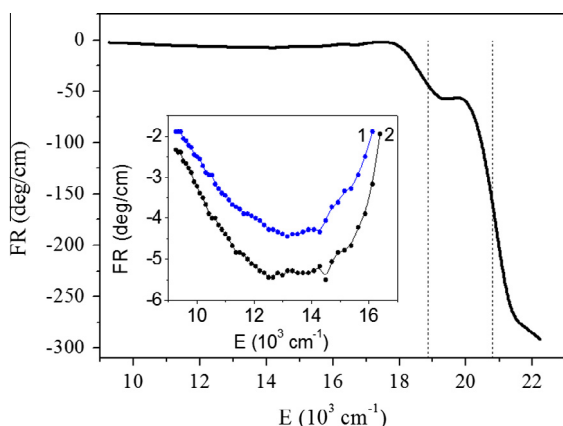
Fig. 9. Room-temperature FR spectrum for sample No. 11 (inset: IR spectral range for samples No. 11 (curve 1) and No. 2 (curve 2)). $B = 0.25$ T.

Fig. 10. The FR values at 700 nm (in relative units) and average nanoparticles size (d) for all samples, Table 1.

with the lowest maximum in the particles size distribution. There is an impression that the FR value is associated with Y. Indeed, Y^{3+} has the lowest ion radius among the doping elements (ion radii are equal to 0.67 for Fe^{3+}, 0.90 for Y^{3+}, 0.96 for Sm^{3+}, 1.03 for Bi^{3+}, and 1.19 Å for Pb^{2+}), therefore it can be incorporated in γ-Fe_2O_3 nanocrystals substituting Fe^{3+} ions in the octahedral positions. Wide FR maximum presented in Fig. 9 (inset) is due to several electron transitions in Fe^{3+} ions occupying both octahedral and tetrahedral positions in accordance with interpretation of MCD spectrum [10]. MCD band centered at 14710 cm^{-1} was ascribed in [10] to the transition $^6A_1(^6S)$–$^4T_1(^4G)$ in the tetrahedral Fe^{3+} ions. So, if Y^{3+} ions

substitute Fe^{3+} ions in octahedral positions the FR value changes in favor of Fe^{3+} in tetrahedral positions.

3.5. EMR

EMR spectra of investigated glasses reveal several components (Fig. 11). In order to interpret the experimental data a computer simulation has been done assuming an ensemble of randomly oriented single-domain ellipsoidal particles dispersed in a diamagnetic matrix with the lognormal diameter and volume distributions. The best fit has been obtained for a superposition of a very narrow symmetrical Lorentzian line with $g \approx 2$ and two relatively wide lines one with g-factor close to 2 (Lorentz-shaped with a resonance field H_1) and another even broader one with $g > 2$ (Gauss-shaped with a resonance field H_2). Fig. 12 presents an example of decomposition of the room-temperature EMR spectra for sample No. 2.

Similar symmetrical narrow line with $g \approx 2$ was observed by several authors for different nanoparticle ensembles [4,22–24]. According to Ref. [4], it is due to very small (~1 nm) Fe oxide nanoparticles and it disappears as particles become larger. The same line was ascribed in Ref. [22] to molecular structures formed by Fe atoms at the interface strongly interacting with the matrix. Thermal fluctuations of magnetic moments and orientations of anisotropy axes were believed to be an origin of this line in the nanoparticles' EMR spectrum [24]. Thus the nature of this line remains ambiguous. The relative weight of this narrow line in the EMR spectra of the investigated glass samples varies from sample to sample and correlates with low-temperature parts of the FC magnetization curves. As it can be seen from Fig. 6 a, the FC magnetization value increases strongly at low-temperatures ($T < 20$ K). Such a behavior differs essentially from the classic magnetization temperature dependence of an ensemble of homogeneous magnetic particles, for example, observed for identical γ-Fe_2O_3 nanoparticles embedded in a polyethylene matrix [1]. The strong increase in magnetization values at low temperatures in our case indicates an abundance of very small particles or paramagnetic ions. The narrow line intensity correlates with the extent of the low-temperature magnetization increase (compare Fig. 11-a and b and Fig. 6-b and c. Note also that the mean particles size in samples Nos. 2 and 11 are equal but the respective maximum FR value at 700 nm in sample No. 11 is higher than that in sample No. 2 (compare curves 1 and 2 in inset of Fig. 9) that additionally justifies a significant amount of Fe present in glass No. 11 as diluted ions or extremely small clusters. A weak narrow line with $g = 4.27$ is observed in some samples at low temperatures. This line is charac-
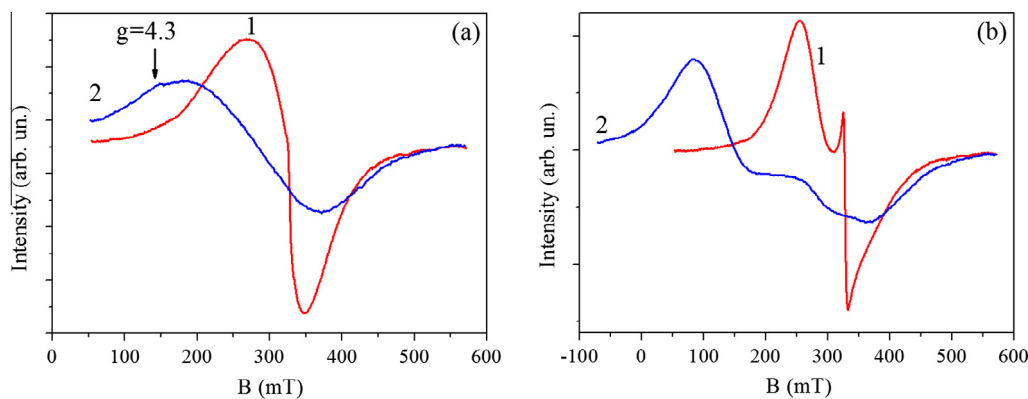
Fig. 11. EMR spectra for samples 2, (a) and 4, (b) at 300 K (curves 1) and 78 K (curves 2).
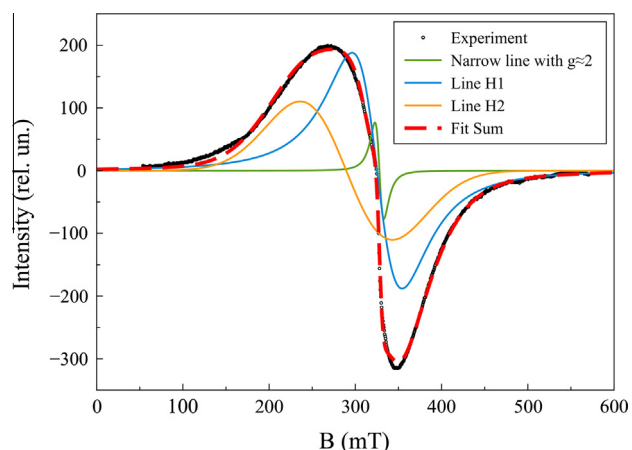

Fig. 12. Room-temperature EMR spectrum decomposition for sample No. 2. (For interpretation of the color lines in this figure, the reader is referred to the web version of this article.)

Table 3
The anisotropy fields at 300 and 77 K for particles of different sizes.

Particles size (nm)	7.6	7.7	7.8	8.0	8.7	9.2	9.6	10.4	11.3	11.6	12.6
H_1–H_2 at 300 K (mT)	41	48.3	58	52	54	38	36	44	52	45	39
H_1–H_2 at 77 K (mT)	84	120	102	75	120	111	69	148	113	174	127

4. Conclusion

Borate glasses co-doped with Fe and large-ion-radius elements (Y, Bi, Pb, and Sm) in different combinations subjected to a specific thermal treatment under identical conditions demonstrate magnetic properties characteristic of magnetically ordered species. Magnetic nanoparticles formation in the glasses was shown to be responsible for their magnetic properties. Only one magnetic phase, γ-Fe_2O_3, has been detected independently of the large radius ions nature. At the same time, doping elements affect in nanoparticle characteristics, including mean size, magnetization, EMR spectra, and magneto-optical effects. In particular, the mean nanoparticle size was found to depend on the doping element concentration ratio: Y and Bi, or Sm and Pb, or Y and Pb, in such a way that there is an optimum concentration of these elements affording glasses with larger magnetic particles. The FR value and particles anisotropy determined from the EMR spectra change from sample to sample analogously to the particles size changes inside each set of co-doping elements.

The sufficiently high FR value in a combination with the low optical absorption in the vicinity of λ = 700–800 nm are the characteristic feature of the glasses investigated what makes them promising materials for magneto-optical applications in the near IR spectral region.

References

[1] S.P. Gubin, Yu.A. Koksharov, G.B. Khomutov, G.Yu. Yurkov, Russ. Chem. Rev. 74 (6) (2005) 489–520.
[2] I. Ardelean, R. Lungu, P. Pascuta, J Mater Sci: Mater Electron. 18 (2007) 837–841.
[3] R. Harizanova, I. Gugov, C. Russel, D. Tatchev, V. Raghuwanshi, A. Hoell, J. Mater. Sci. 46 (22) (2011) 7169–7176.
[4] R. Berger, J. Kliava, J.-C. Bissey, J. Appl. Phys. 87 (2000) 7389–7396.
[5] R. Berger, J.-C. Bissey, J. Kliava, H. Daubric, C. Estournes, J. Magn. Magn. Mater. 234 (2001) 535–544.
[6] R. Berger, J.-C. Bissey, J. Kliava, B. Soulard, J. Magn. Magn. Mater. 167 (1997) 129–135.
[7] J. Kliava, I. Edelman, O. Ivanova, R. Ivantsov, O. Bayukov, E. Petrakovskaja, V. Zaikovskii, I. Bruckental, Y. Yeshurun, S. Stepanov, J. Appl. Phys. 104 (2008) 103917.
[8] I.S. Edelman, T.V. Zarubina, S.A. Stepanov, T.A. Kim, J. Magn. Magn. Mater. 110 (1992) 99–102.

teristic of isolated Fe^{3+} ions in a glass matrix [25], it appears only at low temperatures because of a low concentration of these centers (compare curves for 300 K and 77 K in Fig. 11-a).Thus the data obtained for the narrow line in our samples can be explained according to the model described in [4].

Resonance fields H_1 are almost identical for all samples and temperatures used. Resonance fields H_2 are also close to each other for all samples at room temperature and decrease noticeably as temperature decreases. The difference (H_1–H_2) reflects the anisotropy of particles, which can include several contributions, *e.g.*, intrinsic anisotropy of the crystal structure, surface-induced anisotropy, anisotropy due to shape of particles, anisotropy of interparticle interaction, etc. The (H_1–H_2) values as a function of mean nanoparticle size are summarized in Table 3. One tendency is obvious: the anisotropy increases as temperature decreases, which is expected for the surface-induced contribution. According to Table 3, this contribution is not associated directly with the mean nanoparticles size. The surface anisotropy contribution should decrease as the nanoparticle size increases. It is not supported by experimental observations, which probably means that different samples are characterized by different particle sizes distribution.

[9] H. Akamatsu, J. Kawabata, K. Fujita, Sh. Murai, K. Tanaka, Phys. Rev. B 84 (2011) 144408.
[10] I. Edelman, O. Ivanova, R. Ivantsov, D. Velikanov, V. Zabluda, Y. Zubavichus, A. Veligzhanin, V. Zaikovskii, S. Stepanov, A. Artemenko, J. Curély, J. Kliava, J. Appl. Phys. 112 (2012) 084331.
[11] A.A. Chernyshov, A.A. Veligzhanin, Y.V. Zubavichus, Nucl. Instr. Meth. Phys. Res. A 603 (2009) 95–98.
[12] U. Lembke, A. Hoell, R. Kranold, et al., J. Appl. Phys. 85 (1999) 2279–2286.
[13] O.M. Hemeda, M.Z. Said, M.M. Barakat, J. Magn. Magn. Mater. 224 (2001) 132–142.
[14] R. Hochschild, H. Fuess, J. Mater. Chem. 10 (2000) 539–542.
[15] Myrtil L. Kahn, Z. John Zhang, Appl. Phys. Lett. 78 (2001) 3651–3653.
[16] J.R. Barros, C. Bocker, C. Rüssel, Solid State Sci. 12 (2010) 2086–2090.
[17] E.C. Passamani, C. Larica, C. Marques, J.R. Proveti, A.Y. Takeuchi, F.H. Sanchez, J. Magn. Magn. Mater. 299 (2006) 11–20.
[18] S.P. Pati, A. Roychowdhury, S. Kumar, D. Das, J. Appl. Phys. 113 (2013) 17D708.
[19] R.K. Zheng, G.H. Wen, K.K. Fung, X.X. Zhang, J. Appl. Phys. 95 (2004) 5244.
[20] A.E. Bertkowitz, R.H. Kodama, S.A. Makhlouf, F.T. Parker, F.E. Spada, E.J. McNiff, S. Foner, J. Magn. Magn. Mater. 196–197 (1999) 591–594.
[21] H. Guerrero, G. Rosa, M.P. Morales, F. del Monte, E.M. Moreno, D. Levy, R. Perez del Real, T. Belenguer, C.J. Serna, Appl. Phys. Lett. 71 (1997) 2698–2700.
[22] N. Noginova, F. Chen, T. Weaver, E.P. Giannelis, A.B. Bourlinos, V.A. Atsarkin, J. Phys. Condens. Matter. 19 (2007) 246208.
[23] R.J. Usselman, S.E. Russek, M.T. Klem, M.A. Allen, T. Douglas, M. Young, Y.U. Idzerda, D.J. Singel, J. Appl. Phys. 112 (2012) 084701.
[24] Y.L. Raikher, V.I. Stepanov, Phys. Rev. B 50 (9) (1994) 6250–6259.
[25] I. Ardelean, M. Peteanu, S. Filip, V. Simon, G. Gyorgy, Solid State Commun. 102 (1997) 341–346.